Engineering Structures 243 (2021) 112623

Contents lists available at ScienceDirect

Engineering Structures

journal homepage: www.elsevier.com/locate/engstruct

Significance of multi-hazard risk in design of buildings under earthquake and wind loads

Shinyoung Kwag [a], Abhinav Gupta [b,*], John Baugh [c], Hyun-Su Kim [d]

[a] Department of Civil and Environmental Engineering, Hanbat National University, Daejeon 34158, Republic of Korea
[b] Center for Nuclear Energy Facilities and Structures (CNEFS), Department of Civil, Construction and Environmental Engineering, North Carolina State University, Raleigh, NC 27695, United States
[c] Department of Civil, Construction and Environmental Engineering, North Carolina State University, Raleigh, NC 27695, United States
[d] Division of Architecture, Sunmoon University, Asan-si 31460, Republic of Korea

ARTICLE INFO

Keywords:
Earthquake and wind hazards
Performance-based design
Risk-based multi-hazard approach
Multi-hazard risk map
Multi-hazard scenario
Magneto-rheological damper
Adjacent buildings

ABSTRACT

Traditionally, external hazards are considered in the design of a building through the various combinations of loads prescribed in relevant design codes and standards. It is often the case that the design is governed by a single dominant hazard at a given geographic location. This is particularly true for earthquake and wind hazards, both of which impart time-dependent dynamic loads on the structure. Engineers may nevertheless wonder if a building designed for one of the two dominant hazards will satisfactorily withstand the other. Prior studies have indicated that in some cases, when a building is designed for a single dominant hazard, it does not necessarily provide satisfactory performance against the other hazard. In this paper, we propose a novel framework that builds upon performance-based design requirements and determines whether the design of a building is governed primarily by a single hazard or multiple hazards. It integrates site-dependent hazard characteristics with the performance criteria for a given building type and building geometry. The framework is consistent with the burgeoning area of probabilistic risk assessment, and yet can easily be extended to traditional, deterministically characterized design requirements as illustrated herein.

1. Introduction

Design and retrofit approaches for multi-hazard scenarios have received considerable attention in recent years. However, the concept of multi-hazard analysis is quite broad, and the nature of existing studies varies across a wide spectrum of problems [1,2,3]. In some cases, the focus is on hazards that either occur simultaneously or are closely correlated with one another [4,5,6,7,8,9,10,11,12], such as flooding and fires that are induced by the same seismic event. In other cases, multi-hazard studies relate to hazards that are not dependent or correlated but have a strong likelihood of occurrence at different points in the lifetime of a structure [13,14,15,16,17,18,19]. Design and retrofit assessments for earthquake and extreme wind hazards fall within the latter category.

In the specific case of earthquake and wind loads, design and retrofit solutions are traditionally governed by the requirements of appropriate codes and standards that have historically accounted for multiple hazards through the guidance provided for load combinations. Since performance limit-states in the various codes and standards are the same for loads corresponding to different hazards, the final design is governed by only a single hazard that corresponds to higher loads. The basic premise is that each load combination attempts to account for a scenario that can occur simultaneously. Consequently, much research has been focused on the dynamic behavior of the structures subjected to a single dominant hazard of earthquake or wind [20,21,22,23,24,25,26,27,28]. Also, the design standard ASCE 7-10 recommends using only one of the two, either earthquake or wind hazard, loads in a single load combination. More specifically, the two combinations involving either earthquake or wind are (i) $1.2D + 1.0E + L + 0.2S$ and (ii) $1.2D + 1.0\,W + L + 0.5L_r$, respectively, where D = dead load, E = earthquake load, L = live load, S = snow load, L_r = roof live load, W = wind load. While it is quite evident that the load combination for either earthquake or wind would dominate the design, recent studies have identified the limitations of such an approach. Wen and Kang [30] illustrate that, even if a single

* Corresponding author.
E-mail addresses: skwag@ncsu.edu, skwag@hanbat.ac.kr (S. Kwag), agupta1@ncsu.edu (A. Gupta), jwb@ncsu.edu (J. Baugh), hskim72@sunmoon.ac.kr (H.-S. Kim).

https://doi.org/10.1016/j.engstruct.2021.112623
Received 6 April 2020; Received in revised form 7 March 2021; Accepted 24 May 2021
Available online 9 June 2021

hazard (earthquake or wind) dominates the design loads, the less dominant hazard can contribute significantly to the overall design. Duthinh and Simiu [31] and Crosti et al. [32] additionally show that ASCE 7-05 requirements are not risk-consistent. They illustrate that the overall risk for combined earthquake and wind loads in regions susceptible to both strong earthquakes and extreme winds can be more than twice that calculated by considering only a single dominant hazard. Consequently, these studies propose modifications to ASCE 7-05. Chen [33] considers mid- to high-rise buildings in studying the inherent wind resistance of a building designed for earthquake loads as well as the inherent seismic resistance of a building designed for wind loads. The results indicate that certain solutions for ensuring safety against a single dominant hazard, such as wind, can create competing design objectives with respect to the other hazard, such as an earthquake. Li et al. [34] also show that design and retrofit strategies to improve a structure's performance for withstanding a single hazard can make the structure more vulnerable to other non-dominant hazards.

The fundamental basis for both earthquake and wind design is in finding the appropriate load path through the building and accounting for the dynamic nature of both loads. To do so, designers and engineers may ask if a building designed for one of the two hazards will also perform well for the other. AIA [35] discusses this fundamental question and concludes that the answer is not necessarily so. The study observes that the true answer depends on a building's configuration height, load path for the given structural system, and performance objectives. It also provides an interesting contrast between the two load cases, particularly in the ones calculated from building codes. In particular, earthquake loads calculated using the code provisions are shown to be much less than those typically exhibited during a major earthquake. Ductility of structural members and connections is utilized in the resistance of large earthquake loads, and is achieved through detailing requirements. In contrast, codified wind loads are much closer to the actual loads and wind pressures recorded at a geographic location, and there is no reliance on ductility. Consequently, a design in which inter-story drifts are governed by wind loads will not be able to provide sufficient ductility to withstand a large earthquake. It is targeted that the building under wind load generally remains within an elastic limit. This situation typically arises when buildings are located in regions with low-to-moderate seismicity and strong winds.

In a recent study, Unobe and Sorensen [36] observe that different hazards can dominate performance in different limit states, addressing another aspect of the many possible multi-hazard scenarios. They illustrate that recurring moderate-to-high intensity winds can dominate performance with respect to fatigue, whereas the rare possibility of an earthquake during the lifetime of a structure can dominate the traditional design limit-states in shear, flexure, and/or drifts. This trade-off between competing performance goals, such as those involving earthquakes and winds, has recently garnered considerable attention, and compels us to address multiple hazards in the assessment, design, construction, and retrofit of structures. However, there is in fact no framework available for the designer to determine whether the design of a particular building at a given site is governed by one or more hazards. In this study, the development of such a framework is explored, and a performance-based approach is proposed. The proposed approach makes use of (a) the site-dependent hazard intensity for a given site, (b) the building configuration/height, and (c) performance criteria that govern the design of the building for each individual hazard. The resulting framework can also be used to determine whether a particular building structure requires any retrofitting, especially in cases where both earthquake and wind hazards govern the design and performance of a building whose initial design may not have accounted for them as such. Here, we demonstrate the merits of the proposed framework through an application in which retrofit solutions are examined for two mid- to high-rise buildings located in close proximity to one another, as in a tight urban setting. Results of the analysis show that retrofit solutions differ significantly when evaluated under a multi-hazard scenario.

2. Performance characterization

Structural performance is assessed through the use of limit states, which are characterized by design and serviceability thresholds, and limit states are expressed by performance functions, which can be described in the following form:

$$Z = g(L, R) = L - R \tag{1}$$

where L denotes the performance limit (capacity) of the structure and R represents response (demand) on the structure at a given hazard intensity measure. In general,

$$Z = g(X_1, X_2, ..., X_n) \tag{2}$$

where X_n represents probabilistically defined variables for the loads and the strength. The performance function g is a limit-state function that characterizes the failure criterion as:

$$\begin{array}{l} g(-) < 0 : \text{Failure state} \\ g(-) = 0 : \text{Limit state} \\ g(-) > 0 : \text{Safe state} \end{array} \tag{3}$$

Performance functions are used to determine the safe or failure states from either a deterministic or probabilistic perspective. The probability of failure P_f is then given by the joint probability distribution of X_n's:

$$P_f = \int_{g(-)<0} \cdots \int f_{X_1,X_2,X_3,\ldots,X_n}(x_1, x_2 x_3 \ldots, x_n) dx_1, dx_2, dx_3 \ldots . dx_n \tag{4}$$

where $f_{X_1,X_2,X_3,\ldots,X_n}(x_1, x_2, x_3, \ldots, x_n)$ is the joint probability density function of the random variables.

The performance-based framework we propose is developed for a probabilistic characterization of the performance function, as above. However, limit states are often prescribed deterministically by codes and standards to ensure a minimum level of reliability in the design. Designers evaluate the demand for increasing values of the intensity measure and subsequently determine the value at which Eq. (1) becomes negative for a given capacity, again, as prescribed by relevant codes and standards. As a result, we extend the proposed framework so that it accommodates deterministically characterized performance criteria. It must be noted that different measures are used to quantify the intensity of different hazards, leading to a completely independent characterization of Eq. (1) for different hazards, which cannot be directly compared or combined.

In general, multiple performance limit states exist and are examined in the design of a structure. Yet in most cases, the design is governed by a single performance limit state. Specifically, the performance of the building structure subjected to earthquake loading is typically governed by potentially excessive inter-story drift (characterizing the safety against side-sway collapse). ASCE [29] and [37] building codes specify the limit state for inter-story drift to be 1.5% of the story height. Unlike earthquakes, the design for high wind loading is not governed by the collapse of a building. Instead, it is typically governed by appropriate performance with respect to excessive vibrations, which is characterized in terms of the corresponding serviceability limit state. Tallin and Ellingwood [38] state that the threshold of perception and annoyance for the acceleration intensity is approximately 0.005 g (0.049 m/s^2) ~ 0.015 g (0.147 m/s^2), and the limit for psychological well-being and the ability to perform routine tasks is about 0.04 g (0.39 m/s^2). Recent studies [39,40] presented the latest information on occupant response to wind-induced building motions and the related acceptance criteria. These studies suggested acceptance criteria as follows: 0.005 g is a threshold that is perceptible to occupants and is unlikely to cause significant adverse. 0.01 g is a comfort and well-being threshold that is perceptible to most occupants. 0.035–0.04 g is a fear and safety threshold severe to cause some occupants to lose balance. Besides, excessive acceleration can not only cause discomfort to people but also

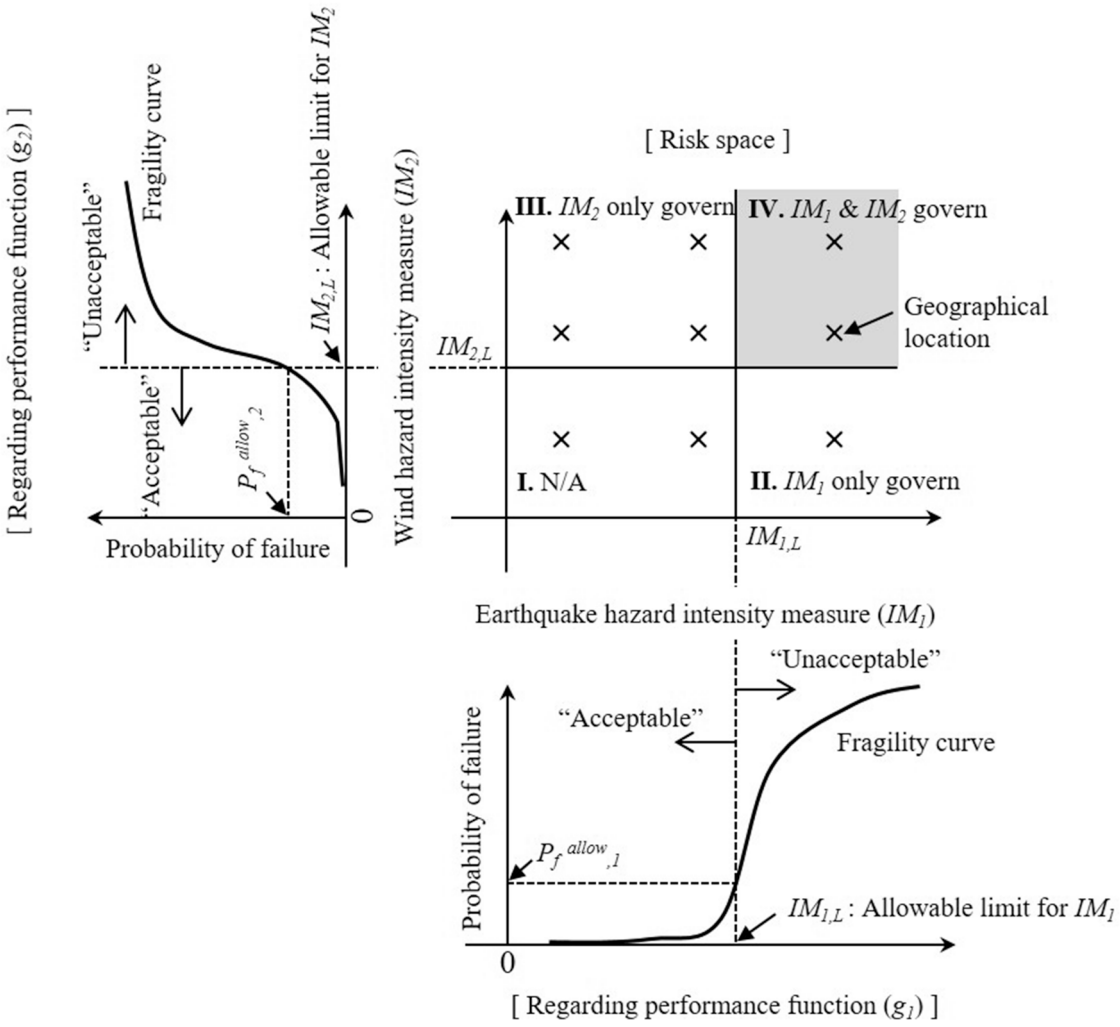

Fig. 1. Graphical representation of proposed framework: multi-hazard risk map.

loss of function to non-structural and electrical equipment [41,42]. For convenience, these limit states are adopted in this study. In general, the two limit states may be expressed as

$$g_1(IM_e) = \mathrm{L_e} - R_e(IM_e) \tag{5}$$

$$g_2(IM_w) = \mathrm{L_w} - \mathrm{R_w}(IM_w) \tag{6}$$

where g_1 is the performance function for earthquakes, which is characterized in terms of the intensity measure for earthquake loading (IM_e); g_2 is a performance function for winds, which is characterized in terms of intensity measure for wind loading (IM_w); $\mathrm{R_e}$ is the maximum inter-story drift (demand) of the structure under earthquake excitation; $\mathrm{L_e}$ is the performance limit (capacity) for earthquake loading, i.e., 1.5% of story height; $\mathrm{R_w}$ is the maximum acceleration (demand) of the structure under wind excitation; $\mathrm{L_w}$ is the performance limit (capacity) for wind loading, i.e., 0.04 g (0.39 m/s^2). Characterizing performance is obviously the essential first step in the development of a performance-based multi-hazard risk assessment framework. In a reliability-based design code, the limit-states are expressed corresponding to an acceptable level of risk. Many design codes continue to evolve and are adopting reliability-based design equations.

3. Proposed framework

3.1. Risk-based multi-hazard approach

The proposed framework combines performance functions with the different intensity measures for multiple hazards in a spatial representation that is subdivided into distinct regions. These graphically depicted regions can then be used to evaluate the significance of each hazard at a given site. Consequently, one of the regions will correspond to sites at which more than a single hazard contributes significantly to the structure's performance.

Fig. 1 shows the proposed graphical framework. As seen in this figure, the starting point is to develop curves of a structure's performance with respect to the intensity measures for each individual hazard. In a probabilistic risk-assessment framework, such curves give the variation of P_f as calculated in accordance with Eq. (4) for a given performance function with the intensity measure for the particular hazard; these are referred to as "fragility curves." As seen in the figure, two fragility curves are plotted with respect to the intensity measures. One curve corresponds to performance function g_1 for earthquakes and the other to g_2 for winds. The feasibility of a design is governed by an acceptable level of risk (or probability of failure), denoted by P_f^{allow}. Such a characterization of the acceptance criterion allows for risk-consistent design among multiple hazards. Safe designs are characterized by $P_f < P_f^{allow}$, whereas failure is characterized by $P_f > P_f^{allow}$. Also, as seen in Fig. 1, the two fragility curves and the definitions of P_f^{allow} for

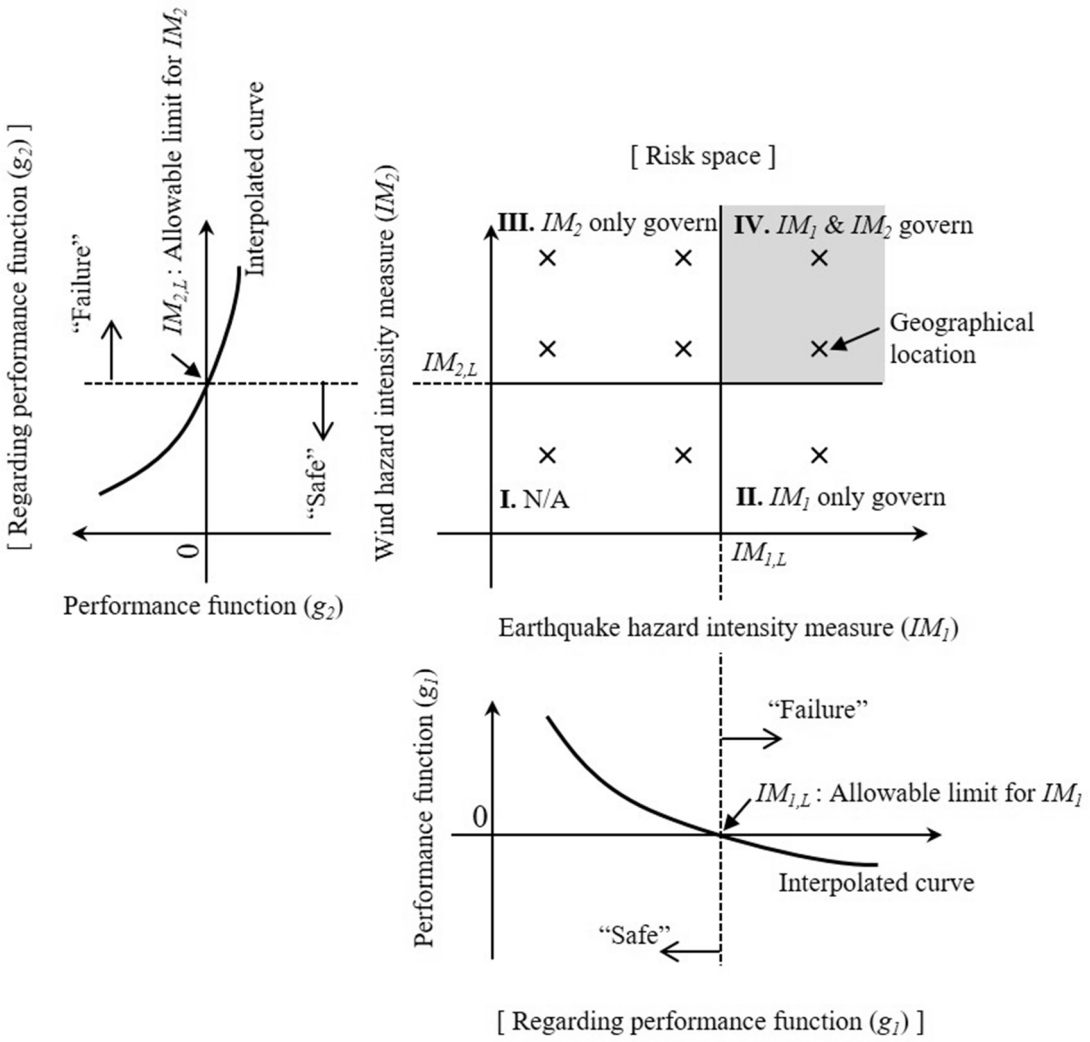

Fig. 2. Development of multi-hazard prone site map: deterministic form.

each hazard are used to develop a third (central) plot, which we refer to as *risk space,* and each axis in this plot represents an intensity measure for one of the hazards. The $P_f^{\,allow}$ value is then used to identify the corresponding intensity measure value ($IM_{1,L}$ and $IM_{2,L}$) in the fragility curve as the limiting boundary in risk space characterized by the corresponding intensity measures. These limiting boundary values, $IM_{1,L}$ and $IM_{2,L}$, are then used to identify four distinct regions in the risk space plot. The region that corresponds to $IM_1 > IM_{1,L}$ and $IM_2 > IM_{2,L}$ is the region in which both the hazards govern the design of the structure. At a given geographical location, the codes and standards can be used to determine the site-specific intensity measures for designing a structure. These two values for the two hazards are represented by a point ("x") in the risk space of Fig. 1, and its location determines whether the design of the particular structures at the given geographic location are governed by both hazards (region IV in Fig. 1) or a single hazard (regions II and III in Fig. 1). The consequence of each hazard is characterized by the corresponding performance criteria which can be different for different hazards. For example, the performance criterion can be the safety against a side-way collapse in the case of earthquakes, whereas, for wind hazard, the performance criterion can be the serviceability limit of the occupant's safe mobility. Next, the framework presented in Fig. 1 is transformed into a performance-based framework in order to allow practical applications.

3.2. Transformation of risk based approach to performance based approach

The risk-consistent framework proposed above is developed while keeping in mind the actively evolving area of probabilistic risk assessment and reliability-based design. While the framework presented in Fig. 1 above is based on fundamental principles, its application to actual design or retrofit assessment studies is not straightforward and in some cases impractical due to the complexity and cost of evaluating fragility curves. For practical applications, the framework presented above can be converted into a simpler deterministic performance-based form. The performance-based form provides consistency with current design codes and standards. As shown in Fig. 2, a modified form of Fig. 1, the fragility curves are replaced with deterministically generated curves for g_1 and g_2 with respect to their intensity measures. The performance functions g_1 and g_2 are deterministic in nature as per Eq. (5) and (6), discussed earlier. The limiting values of intensity measures $IM_{1,L}$ and $IM_{2,L}$ in this form correspond to $g_1 = 0$ and $g_2 = 0$, respectively. The subsequent definition of risk space and identification of different regions remains identical to that of Fig. 1. Specifically, the four regions can be described as: I. sites at which the initial/current design is acceptable with respect to both the hazards when $g_1 > 0$ and $g_2 > 0$; II. sites governed by only earthquake hazard when $g_1 \leq 0$ and $g_2 > 0$; III. sites governed by only wind hazard when $g_1 > 0$ and $g_2 \leq 0$; IV. sites governed by both earthquake and wind hazards when $g_1 \leq 0$ and $g_2 \leq 0$.

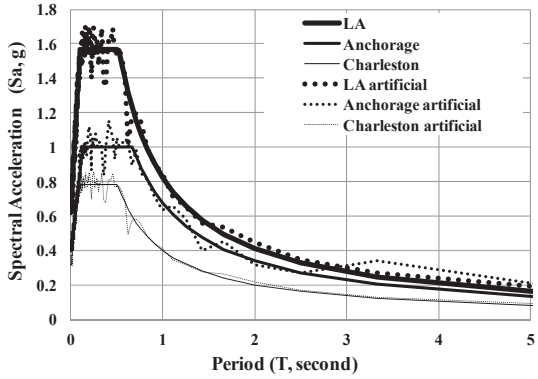

Fig. 3. Design spectra and compatible ground motions.

4. Illustration of proposed framework

In this section, we illustrate the development and utilization of the proposed framework through a simple example that includes several selected geographic locations. This example shows the effectiveness of this proposed framework and the proposed framework's utilization by extending to structural retrofit. As discussed above, it uses the risk consistent performance-based concept presented in Fig. 2 above which in turn has its roots in the fundamental multi-hazard risk framework presented in Fig. 1 through the use of performance functions for probabilistic risk results. For simplicity, a square cross-section of the building is considered with width B = 16 m and story height h = 4 m. To begin, a 20-story (80 m) building is considered, and the illustration is then extended to 30-story (120 m) and 40-story (160 m) buildings. The buildings exhibit slenderness with a total height (H = 80 m, 120 m, 160 m) to width (B) ratio of 5–10. The mass of each floor is taken as 8e5 kg and the inter-story stiffness is taken as 1.4e9 N/m. The performance functions for this structure become $g_1 = 0.06 - R_e$ (unit in m, $L_e = 1.5\%$ of 4 m = 0.06 m) for an earthquake loading and $g_2 = 0.39 - R_w$ (unit in m/s^2, $L_w = 0.04$ g = 0.39 m/s^2) for a wind loading by adopting Eq. (5) and Eq. (6). In order to outline the process of characterizing hazards and developing input loadings, three representative geographical locations are considered: (i) Los Angeles, CA (ii) Anchorage, AK and (iii) Charleston, SC. The primary reason for selecting these specific locations is that all three sites are vulnerable to seismic and wind hazards.

4.1. Characterization of earthquake hazard

The USGS (United States Geological Survey) and ASCE 7-10 provide seismic hazard intensity measures which are characterized in terms of the mapped hazard spectral accelerations at short period (S_S) and 1 s period (S_1). ASCE 7-10 requires that the mapped hazard values (S_S and S_1) be multiplied by the site-specific soil amplification coefficients (F_a and F_v) and the design reduction factor (2/3) for characterizing the design hazard parameters (S_{DS} and S_{D1}). These parameters are then used to construct the design spectrum. If an acceleration time history is needed for the analysis of structural responses, the design spectrum is used to develop corresponding motions by scaling the historical ground motions or artificially generating ground motions compatible with the design spectrum.

Next, we apply this process to characterize the seismic hazard at the three selected sites in this study. For Los Angeles, it is determined that S_S = 2.348 g and S_1 = 0.823 g. For Anchorage, S_S = 1.500 g and S_1 = 0.676 g, and for Charleston, S_S = 1.119 g and S_1 = 0.355 g. For comparison purposes, we consider the same soil site classification (class D) for the local soil profile. The soil amplification factors are F_a = 1 and F_v = 1.5 for Los Angeles, F_a = 1 and F_v = 1.502 for Anchorage, and F_a = 1.052 and F_v = 1.609 for Charleston. The design hazard parameters with a soil site class D are calculated to be S_{DS} = 1.565 g and S_{D1} = 0.823 g for Los Angeles, S_{DS} = 1.000 g and S_{D1} = 0.676 g for Anchorage, and S_{DS} = 0.785 g and S_{D1} = 0.400 g for Charleston. Fig. 3 shows the design spectra calculated at these sites in accordance with ASCE 7-10 and represented by solid lines in the figure. For analysis purposes, the spectrum compatible artificial ground motions for each site are generated as described in Gasparini and Vanmarcke [43]. The response spectra calculated from the artificial ground motions are shown by the dashed lines in Fig. 3. The artificial time histories for each of the three sites are shown in Fig. 4.

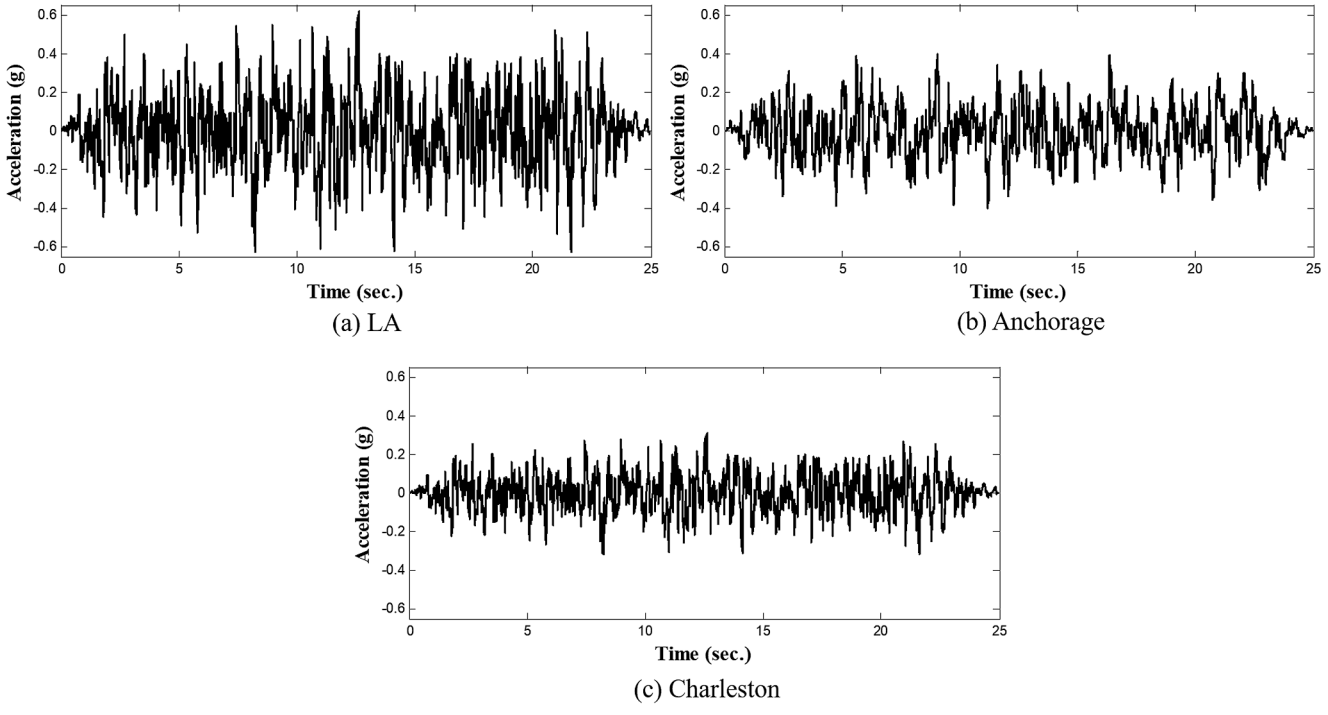

Fig. 4. Design spectra compatible ground motions.

4.2. Characterization of wind hazard

ASCE 7-10 gives wind speed maps for the entire United States that can be used to calculate the wind hazard. Static wind pressure is determined from the basic wind speed (V), which is considered to act as a three-second gust speed at 10 m above the ground in a particular exposure category (c). This information is then used to determine the importance factor (I), exposure coefficient (K_z), topographical factor (K_{zt}), and wind directional factor (K_d) in order to calculate the design velocity pressure (q_z) at height (z) as follows:

$$q_z = 0.613 K_z K_{zt} K_d V^2 I \left(N/m^2\right) \tag{7}$$

This study is aimed at the wind loading generated along the wind. Wind time history loadings can be developed by using the Kaimal spectrum as described below in Eq. (8) and (9).

$$\frac{fS_u(z,f)}{\sigma_u^2} = \frac{6.8 f_L}{\left(1 + 10.2 f_L\right)^{5/3}} \tag{8}$$

$$f_L = \frac{f L_H(z)}{U_H(z)} \tag{9}$$

where f is frequency; z is height; S_u is power spectral density of the longitudinal velocity. f_L is height dependent length scale of turbulence (reduced frequency); σ_u is the standard deviation; L_H is a length scale of longitudinal turbulence; U_H is wind velocity evaluated at the height. To take the correlation of all stories of the building into account, the defined spectrum should be updated by the following equation:

$$S_{rs} = \sqrt{S_{rr}(f) S_{ss}(f)} \cdot \exp\left[-f \frac{k_z |z_r - z_s|}{(1/2)[U_H(z_r) + U_H(z_s)]} \right] \tag{10}$$

where S_{rr} and S_{ss} are wind velocity spectra for stories r and s, respectively; S_{rs} is the off-diagonal wind velocity spectrum considering the correlation between stories r and s; k_z is the decay constant; z_r is the height of story r; z_s is the height of story s. The decay constant considering the cross-correlation for obtaining off-diagonal spectra is typically taken as 10 when generating wind time history loadings. The transformation from the spectrum to a time history [44,45,46] can be performed in three steps: (1) the lower triangle matrix is obtained via Cholesky decomposition, (2) the FFT (Fast Fourier Transformation) function (X_p) having a phase angle following a normal distribution is generated at each floor, (3) the wind time histories (x_p) at each floor are obtained by using the inverse FFT operation. The equations for X_p and x_p are as follows:

$$X_p(k\Delta f) = \sqrt{2 f_c N} \sum_{i=1}^{p} H_{pi}(k\Delta f) \zeta_{ik} \tag{11}$$

$$x_p(n\Delta t) = \frac{1}{N} \sum_{k=0}^{N-1} X_p(k\Delta f) exp\left(i \frac{2\pi k n}{N} \right) \tag{12}$$

where H_{pi} is the lower triangle matrix; ζ_{ik} is a complex Gaussian random variable having a mean of 0 and variance of 0.5; Δt is $1/(2 \cdot f_c)$; f_c is the Nyquist frequency; Δf is a useful frequency increment for FFT data; N is a total number of points in the time series; p is a floor of the structure; i is an imaginary number.

Next, we apply the wind loading characterization described above to the three representative geographical locations considered in this study. To begin with, the basic wind speeds for the three sites of Los Angeles, Anchorage, and Charleston are taken as 38 m/s, 54 m/s, and 63 m/s, respectively, from the code-defined wind speed map. Other conditions of the exposure category, I, K_{zt} and K_d are taken as Exposure C, 1.0, 1.0, and 0.85, respectively. The value of K_z can be obtained from the code-defined shape along the height of the building structure. Based on these values and the simple 20-story building structure considered, the wind time history loadings are generated artificially for a total duration

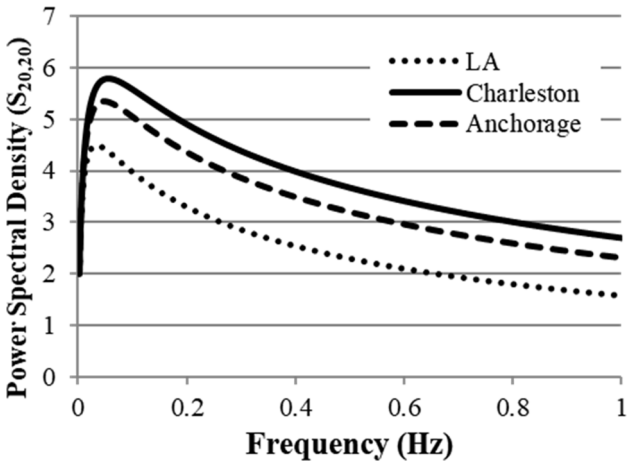

Fig. 5. PSD curves of wind velocity at the 20th floor of 20-story building ($S_{20,20}$ (f)).

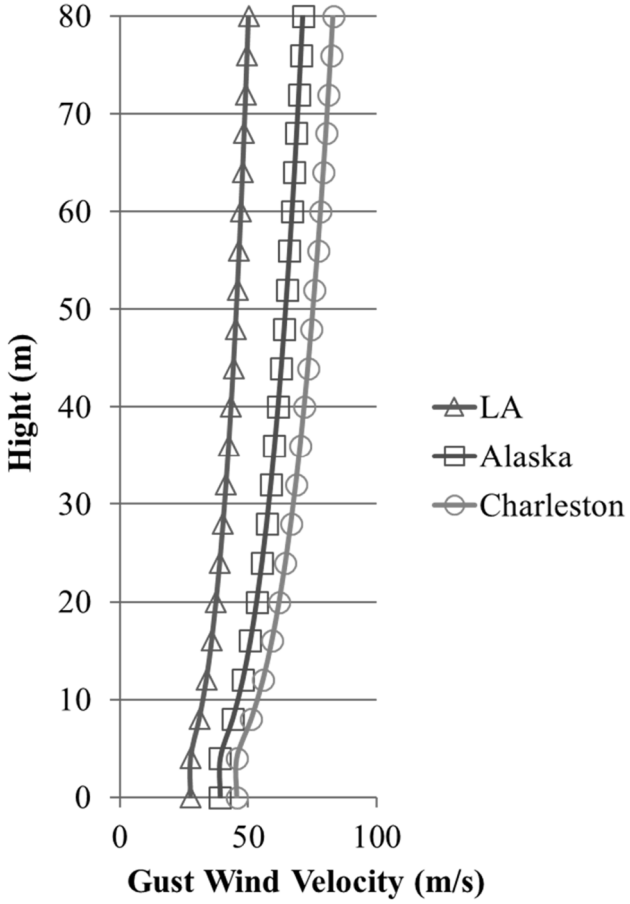

Fig. 6. Gust wind velocity distribution with height.

of 300 s at a time step of 0.5 s. The power spectrum density (PSD) curves of wind velocity of $S_{20,20}$ are calculated using Eq. (10) and are illustrated in Fig. 5. The gust wind velocity distributions over the height of the 20-story building structure are specified in Fig. 6. Fig. 7 shows the story wind time history loadings generated at the top floor of the 20-story building structure for each of the three sites. These story wind time history loadings are obtained by subtracting the loadings caused by each floor's gust wind speed from the total wind loadings and generating only the fluctuating wind loadings. The generated story wind time-history

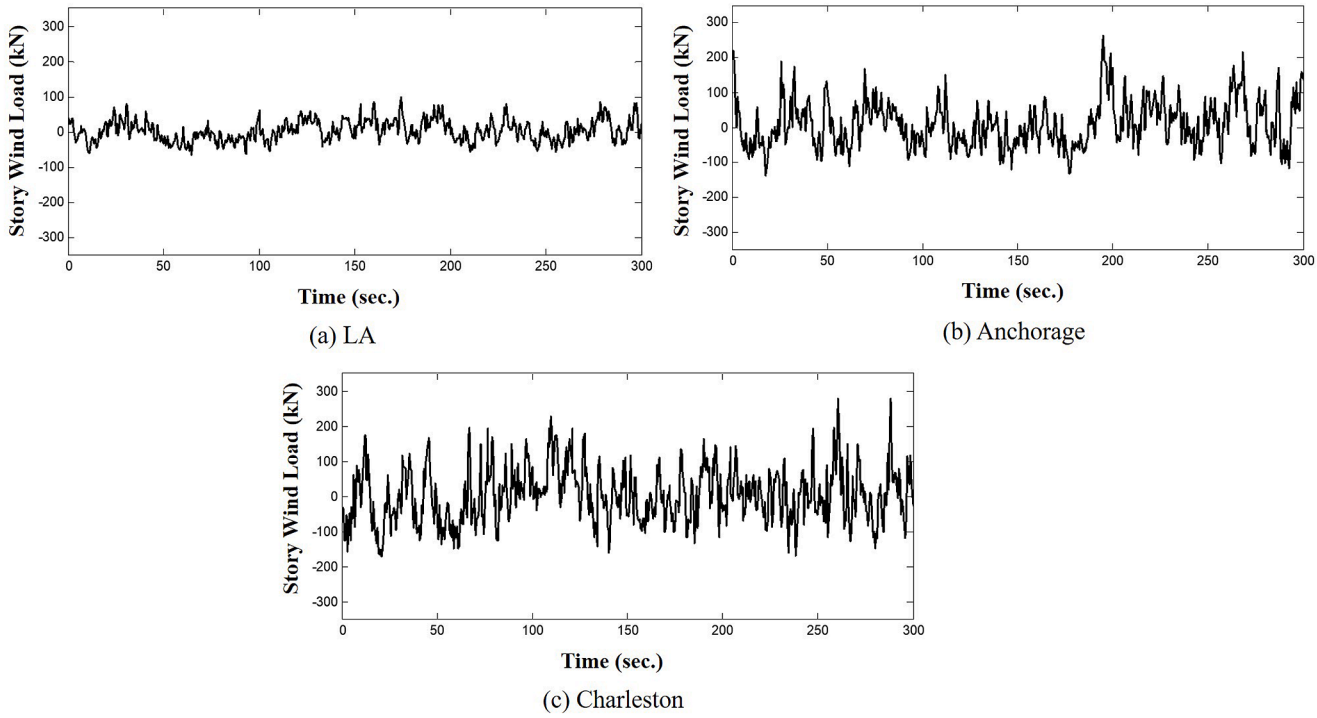

Fig. 7. Story wind time history loadings at the top floor of the 20-story building.

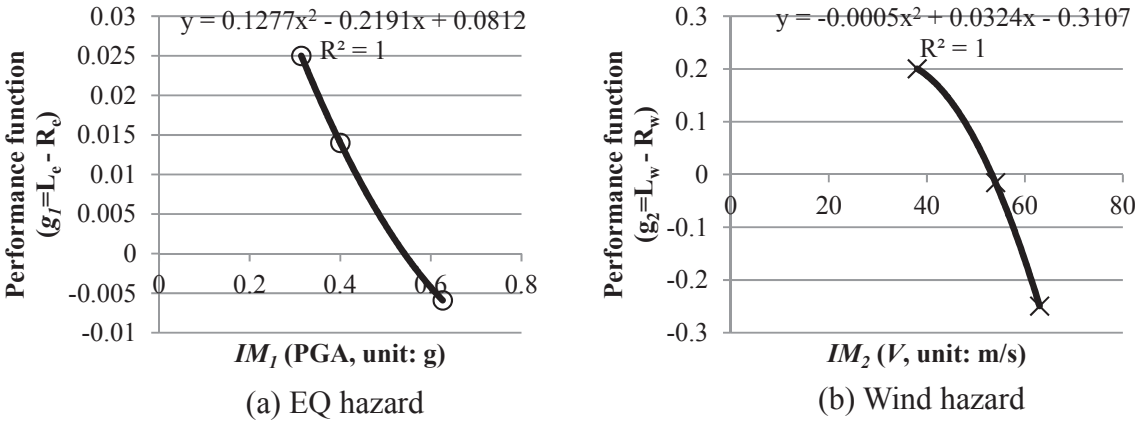

Fig. 8. Evaluated performance function values of 20-story building structure and interpolated curves under two hazard intensity measures of EQ and Wind for three representative sites.

loadings act as lateral forces at the lumped mass point of each floor.

4.3. Development of multi-hazard risk map

In this study, we consider the intensity measures for earthquake and wind (IM_1 and IM_2) as peak ground acceleration (PGA) and basic wind speed (V). For the 20-story building, the performance function is characterized as inter-story drift for earthquake, and along-wind acceleration for wind, in order to quantify functions g_1 and g_2. The performance functions are calculated at the three sites for a suite of IM_1 and IM_2 values, and corresponding interpolated curves for these performance functions are found by the regression analyses. The corresponding curves for g_1 versus PGA and g_2 versus V are shown in Fig. 8. As seen in these curves, the failure limits for each hazard intensity measure are found to be 0.54 g ($IM_{1,L}$) for earthquake and 53 m/s ($IM_{2,L}$) for wind. With these values of $IM_{1,L}$ and $IM_{2,L}$, we now plot risk space and identify the four distinct regions of multi-hazard risk in Fig. 9. Finally, coordinates for the three sites (Los Angeles, Anchorage, and Charleston) are located in risk space to determine the significance of single versus multiple hazards in the design of this 20-story building. For instance, if this 20-story building is located at a site where the design levels are>0.54 g for earthquakes but less than 53 m/s for winds, then its design is governed by only the earthquake hazard. On the other hand, if the structure is located at a site where the design levels of both hazards are greater than 0.54 g and 53 m/s, its design will be governed by both hazards.

Finally, we illustrate the changing nature of risk space as developed in the proposed framework by considering 30-story and 40-story buildings. The story height and slenderness ratio for each building are taken to be the same as before, i.e., the story height is 4 m and slenderness ratio is 5. The same process is repeated for each building and the corresponding risk space plotted, with the results for all three buildings shown in Fig. 10. We observed that, as the total height of the building is increased, many more geographical locations fall under the region

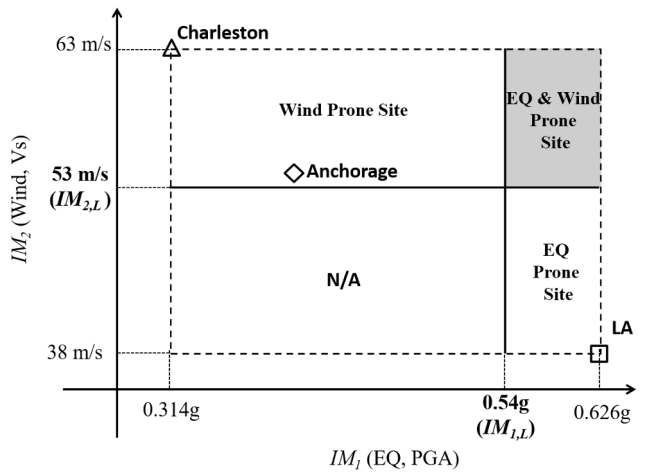

Fig. 9. Risk space: multiple hazard prone site map for 20-story building structure.

where $g_1 \leq 0$ and $g_2 \leq 0$, indicating an increased susceptibility to multiple hazards.

In the following section, we illustrate that the proposed multi-hazard-based framework can lead to different solutions. For visualization of such variations in proposed solutions, we consider two buildings located in close proximity of one another and are connected by supplemental damping devices as a retrofit solution. This particular application is taken from published literature in which solutions are evaluated for the case of only a single earthquake hazard. The motivation for selecting this example lies in its ability to help the reader visualize that the solutions are very different in the case of single hazard of purely wind and purely earthquake by themselves and both of these solutions are quite different from the one evaluated by consideration of a multi-hazard scenario.

5. Application: Alternative solutions in a multi-hazard scenario

For this application of the framework, we consider a 20-story building located in close proximity to a 10-story building in a tight urban setting. This particular example appears in the literature [20,22] in the context of earthquake design for adjacent buildings connected by supplemental damping devices. At the same time, the concept of connecting adjacent buildings by supplemental damping devices has also been presented as a possible approach for withstanding high winds [23]. Therefore, we examine the implications of a multi-hazard scenario for this example application.

Fig. 11 shows the configuration of two adjacent buildings connected by supplemental damping devices at different floor levels. The actual floor levels and the number of damping devices needed at each floor are investigated in determining the retrofit solution for these buildings. The buildings are assumed to be located at a geographical location that corresponds to an earthquake intensity measure similar to one in Los Angeles and a wind intensity measure similar to one in Charleston. With respect to supplemental damping devices, many different types are available and can be used, such as metallic, friction dampers, viscoelastic dampers, tuned-mass dampers, isolators, and MR-dampers. For the purpose of this study, we consider MR-dampers since Ok et al. [22] use MR dampers in their study for earthquake loads. Similarly, Kim and Kang [24] utilize MR dampers for high winds. Prior to evaluating design alternatives for a multi-hazard scenario with MR dampers, we present the numerical model for MR dampers that are used in conducting the analysis in the next section. The following section also presents a brief discussion of the design parameters used for characterizing the MR dampers.

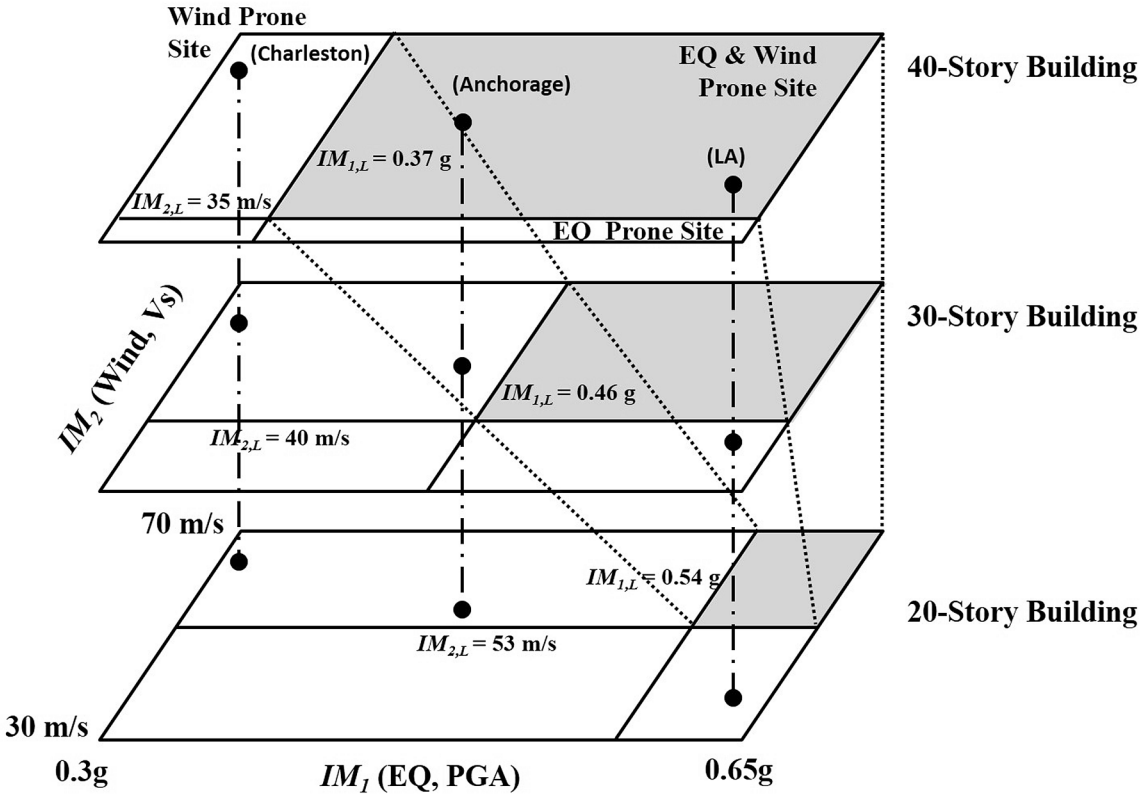

Fig. 10. Change of multi-hazard prone area according to total heights of building.

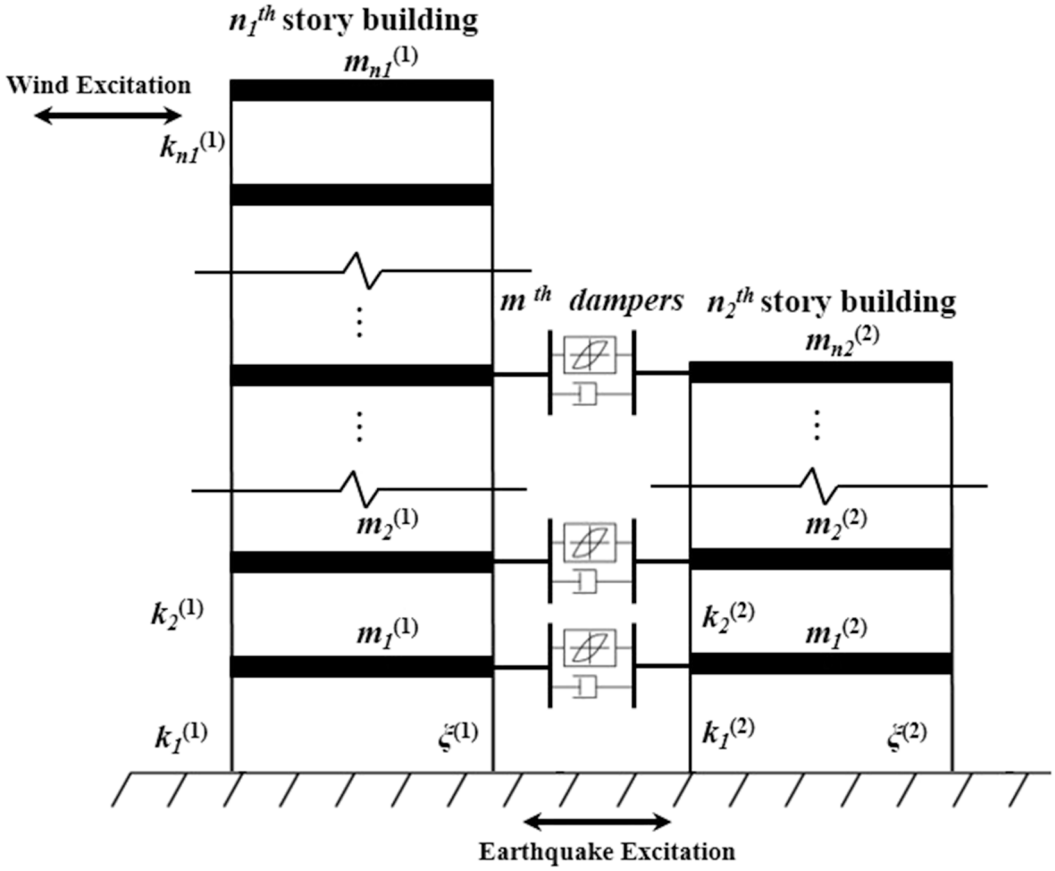

Fig.11. Coupled buildings connected with nonlinear hysteretic MR dampers.

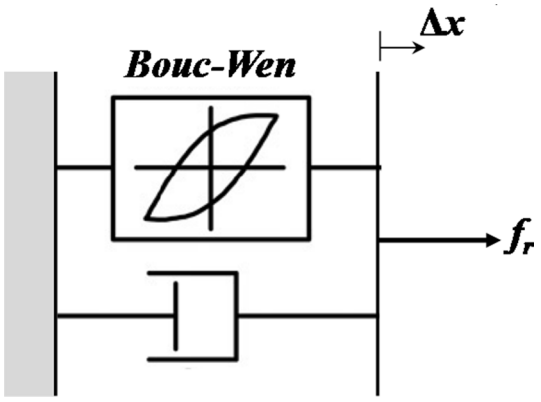

Fig. 12. MR damper mechanical model.

5.1. Numerical model of MR damper

Several mechanical models have been proposed over the years to model MR damper behavior [47]. In this study, we adopt the experimentally validated model shown in Fig. 12 that uses a Bouc-Wen element and a viscous damper in parallel [48]. The restoring force in this model is expressed as shown below in Eq. (13). As seen in this equation, the restoring force f_r is composed of linear viscous elastic and hysteretic parts:

$$f_r = c_0 \Delta\dot{x} + \alpha y \tag{13}$$

$$c_0(V) = c_{0a} + c_{0b} V \tag{14}$$

$$\alpha(V) = \alpha_a + \alpha_b V \tag{15}$$

where the parameters c_0 and α represent the viscous damping and inelastic coefficients, respectively; Δx is the nonlinear element-ended relative displacement; $\Delta\dot{x}$ is the nonlinear element-ended relative velocity; and y is the interior hysteretic variable, which is expressed as the first-order nonlinear differential equation given by Eq. (16):

$$\dot{y} = -\gamma|\Delta\dot{x}|y|y|^{n-1} - \beta\Delta\dot{x}|y|^n + A\Delta\dot{x} \tag{16}$$

where the parameter A controls the scale of the hysteresis loops and n determines the sharpness of the hysteresis cycle in the region of change from the elastic to the inelastic part; β and γ are parameters that control the shape of the hysteretic behavior [49].

In this study, we choose an MR damper of capacity approximately equal to 100 kN that has the following set of parameters characterizing its behavior based on experimental studies [50], i.e., $c_{0a} = 0.88e2$ N-s/cm, $c_{0b} = 8.8e2$ N-s/cm/V, $\alpha_a = 21744e2$ N/cm, $\alpha_b = 99232e2$ N-s/cm/V, $\gamma = 3\ \text{cm}^{-1}$, $\beta = 3\ \text{cm}^{-1}$, $A = 1.2$, and $n = 1$. Fig. 13 illustrates the force-velocity/displacement hysteretic behaviors of this particular MR damper model for six different input voltage values. The input voltage determines the maximum damping force and the energy dissipation. Therefore, the input voltage is a key parameter needed in determining the retrofit solution. The input voltage determines its force behavior, which in turn governs the number of dampers needed in a given design alternative.

Next, we describe the mathematical model that represents the equations of motion for two buildings coupled with MR-dampers. This mathematical model is needed for conducting an analysis with earthquake and wind loads.

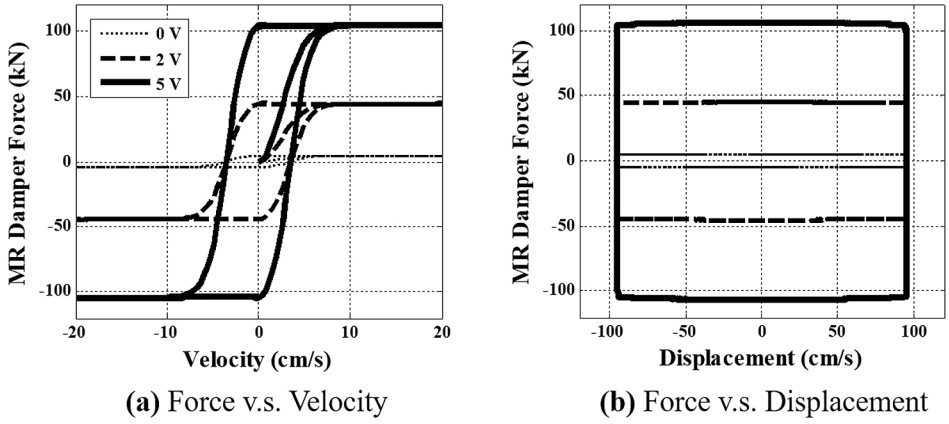

Fig. 13. Nonlinear hysteretic behavior of the MR damper.

5.2. Mathematical model for coupled buildings with MR dampers

Fig. 11 illustrates two adjacent buildings with n_1^{th} and n_2^{th} stories ($n_1 > n_2$) connected by m nonlinear hysteretic MR dampers along floors in the horizontal direction. Under earthquake and wind excitations, it is assumed that the coupled buildings remain linearly elastic, whereas the dampers experience nonlinear hysteretic behavior and transfer damper forces to the connecting floors of the buildings. The governing equations of motion for shear-type coupled building models ($N = n_1 + n_2$) are expressed as:

$$[M]\{\ddot{u}\} + [C]\{\dot{u}\} + [K]\{u\} + \{F_d\} = \{f\} \tag{17}$$

$$\{F_d\}_{N\times 1} = [C_0]_{N\times N}\{\dot{u}\}_{N\times 1} + [\mathrm{A}]_{N\times n_2}\{y\}_{n_2\times 1} \tag{18}$$

$$[M]_{N\times N} = \begin{bmatrix} [M^{(1)}]_{n_1\times n_1} & [0]_{n_1\times n_2} \\ [0]_{n_2\times n_1} & [M^{(2)}]_{n_2\times n_2} \end{bmatrix} \tag{19}$$

$$[C]_{N\times N} = \begin{bmatrix} [C^{(1)}]_{n_1\times n_1} & [0]_{n_1\times n_2} \\ [0]_{n_2\times n_1} & [C^{(2)}]_{n_2\times n_2} \end{bmatrix} \tag{20}$$

$$[K]_{N\times N} = \begin{bmatrix} [K^{(1)}]_{n_1\times n_1} & [0]_{n_1\times n_2} \\ [0]_{n_2\times n_1} & [K^{(2)}]_{n_2\times n_2} \end{bmatrix} \tag{21}$$

$$[C_0]_{N\times N} = \begin{bmatrix} diag[c_0]_{n_2\times n_2} & [0]_{n_2\times(n_1-n_2)} & -diag[c_0]_{n_2\times n_2} \\ [0]_{(n_1-n_2)\times n_2} & [0]_{(n_1-n_2)\times(n_1-n_2)} & [0]_{(n_1-n_2)\times n_2} \\ -diag[c_0]_{n_2\times n_2} & [0]_{n_2\times(n_1-n_2)} & diag[c_0]_{n_2\times n_2} \end{bmatrix} \tag{22}$$

$$[\mathrm{A}]_{N\times n_2} = \begin{bmatrix} -diag[\alpha]_{n_2\times n_2} \\ [0]_{(n_1-n_2)\times n_2} \\ diag[\alpha]_{n_2\times n_2} \end{bmatrix} \tag{23}$$

where $[M]$, $[C]$, and $[K]$ represent the $N \times N$ dimensional mass, damping, and stiffness matrices of the coupled buildings, respectively; the superscripts (1) and (2) denote the n_1^{th} and n_2^{th} story buildings; $\{u\}$, $\{\dot{u}\}$, and $\{\ddot{u}\}$ are the $N \times 1$ dimensional displacement, velocity, and acceleration vectors; $\{F_d\}$ denotes the $N \times 1$ dimensional force vector induced by nonlinear hysteretic MR dampers; $\{f\}$ denotes the $N \times 1$ dimensional force vector caused from external earthquake or wind excitations; $[C_0]$ and $[\mathrm{A}]$ indicate the $N \times N$ dimensional damping and $N \times n_2$ dimensional inelastic coefficient matrices, respectively. In order to obtain responses of the system with respect to the force vector, we represent the equation of motion given by Eq. (17) as the second-order ordinary differential equation (ODE) given by Eq. (24), and describe the second-order ODE of Eq. (24) by a first-order ODE representation of Eq. (25a):

$$\begin{gathered} \{\dot{u}\} = [I]\{\dot{u}\} \\ \{\ddot{u}\} = -[M]^{-1}[K]\{u\} - [M]^{-1}[C]\{\dot{u}\} - [M]^{-1}[C_0]\{\dot{u}\} - [M]^{-1}[\mathrm{A}]\{y\} + [M]^{-1}\{f\} \\ \{y\} = \left\{-\gamma|\Delta\dot{u}|y|y|^{n-1} - \beta\Delta\dot{u}|y|^n + A\Delta\dot{u}\right\} \end{gathered} \tag{24}$$

$$\left\{\dot{Y}\right\} = f(t, \{Y\}) \tag{25a}$$

$$\begin{aligned} \{Y\}_{(2N+m)\times 1} \left(\right. &= [\, Y_1 \sim Y_N \quad Y_{N+1} \sim Y_{2N+1} \quad Y_{2N+1} \sim Y_{2N+m}\,]^T \left. \right) \\ &= [\, \{u\}^T_{N\times 1}\{\dot{u}\}^T_{N\times 1}\{y\}^T_{m\times 1}\,] \end{aligned} \tag{25b}$$

$$\begin{Bmatrix} \dot{Y}_{N+1} \\ \vdots \\ \dot{Y}_{2N} \end{Bmatrix} = -[M]^{-1}[K]\begin{Bmatrix} Y_1 \\ \vdots \\ Y_N \end{Bmatrix} - [M]^{-1}[C]\begin{Bmatrix} Y_{N+1} \\ \vdots \\ Y_{2N} \end{Bmatrix} - [M]^{-1}[C_0]\begin{Bmatrix} Y_{N+1} \\ \vdots \\ Y_{2N} \end{Bmatrix} - [M]^{-1}[\mathrm{A}]\begin{Bmatrix} Y_{2N+1} \\ \vdots \\ Y_{2N+m} \end{Bmatrix} + [M]^{-1}\{f\} \tag{25d}$$

$$\begin{Bmatrix} \dot{Y}_{2N+1} \\ \vdots \\ \dot{Y}_{2N+m} \end{Bmatrix} = \begin{Bmatrix} -\gamma|(Y_{N+n_1+1} - Y_{N+1})\,|Y_{2N+1}|Y_{2N+1}|^{n-1} - \beta(Y_{N+n_1+1} - Y_{N+1})|Y_{2N+1}|^n + A(Y_{N+n_1+1} - Y_{N+1}) \\ \vdots \\ -\gamma|(Y_{N+n_1+m} - Y_{N+m})\,|Y_{2N+m}|Y_{2N+m}|^{n-1} - \beta(Y_{N+n_1+m} - Y_{N+m})|Y_{2N+m}|^n + A(Y_{N+n_1+m} - Y_{N+m}) \end{Bmatrix}$$

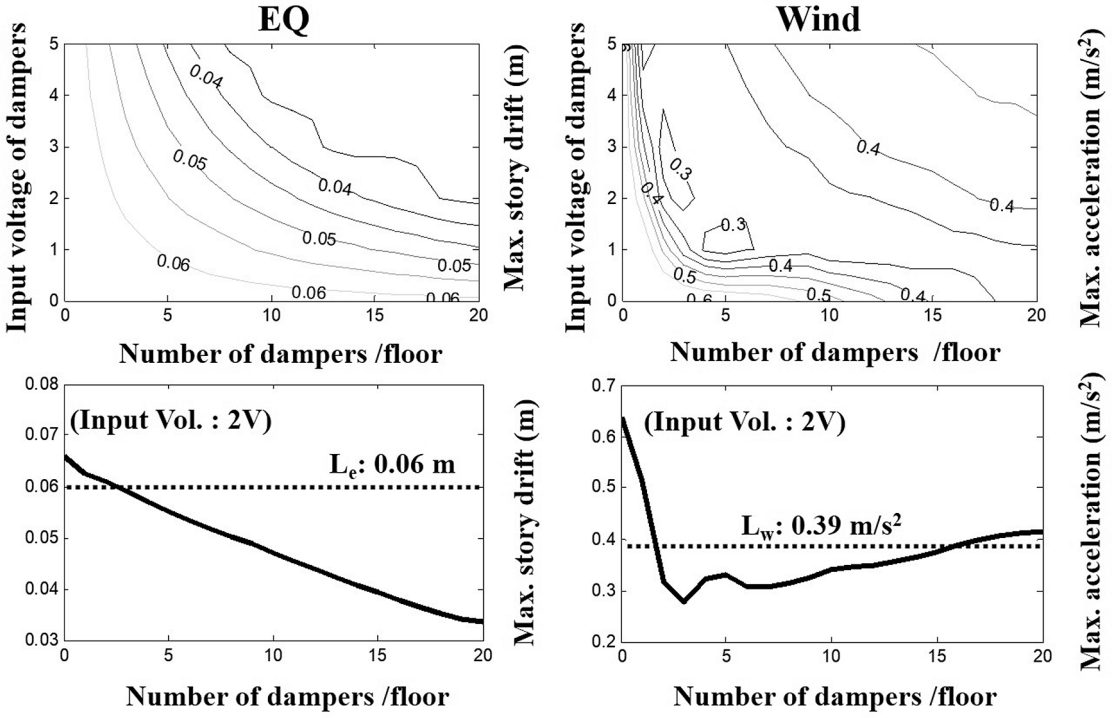

Fig. 14. Installing MR dampers at all floors uniformly (all floors).

$$\left\{\dot{Y}\right\}_{(2N+m)\times 1}\left(=\left[\dot{Y}\sim\dot{Y}_N\dot{Y}_{N+1}\sim\dot{Y}_{2N}\dot{Y}_{2N+1}\sim\dot{Y}_{2N+m}\right]^T\right)$$
$$=\left[\{\dot{u}\}^T_{N\times 1}\{\ddot{u}\}^T_{N\times 1}\{\dot{y}\}^T_{m\times 1}\right] \quad (25c)$$
$$\left\{\begin{matrix}\dot{Y}_1\\ \vdots\\ \dot{Y}_N\end{matrix}\right\}=[I]_{N\times N}\left\{\begin{matrix}Y_{N+1}\\ \vdots\\ Y_{2N}\end{matrix}\right\}$$

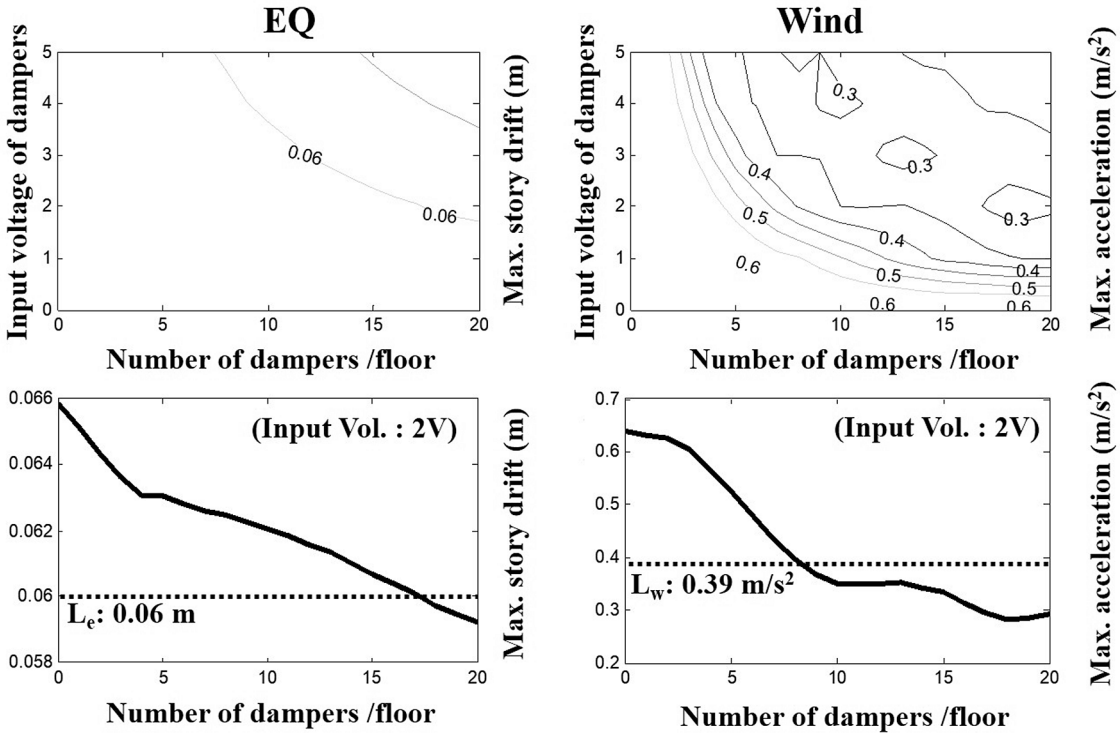

Fig. 15. Installing MR dampers at single floor (at top of 10-story building).

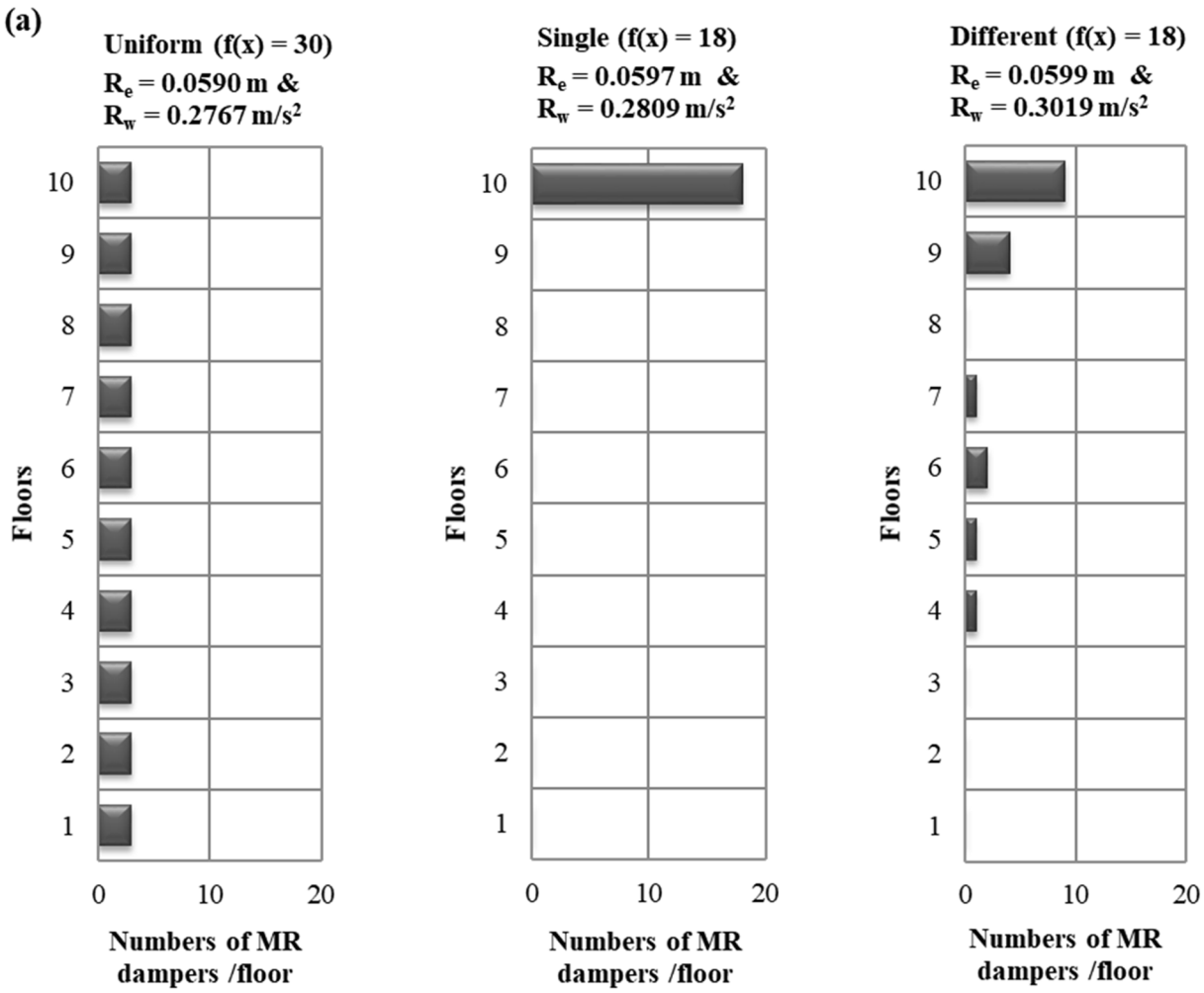

Fig. 16. Distribution of the numbers of MR damper along floors under a uniform 2 V input voltage signals: (a) uniformly installed at all floors (case 1); (b) installed at a single story (case 2); (c) differently installed at all floors (case 3).

where $\{Y\}$ is the space-state vector. The detailed components of the state vector and the first-order ODE are described in Eq. (25b) to Eq. (25d). Eq. (25a) is solved using the fourth-order Runge-Kutta algorithm. The $f(-)$ in Eq. (25a) is expressed in the second mathematical expression of Eq. (25d). This is a fully expressed governing equation of the matrix-form of a first-order ODE.

Specifically for this study, $n_1 = 20$ and $n_2 = 10$. The properties of the 20-story building are the same as those described in section 4, and the building's performance depends on where it is as per the risk space of the proposed framework presented in section 4.3. The 10-story building has a square cross-section with 8 m width (B), 4 m story height, and a slenderness ratio of 5. The mass of each floor is 8e5 kg and the inter-story stiffness is 1.4e9 N/m. The first five natural frequencies of the 20-story building structure alone are 0.51, 1.52, 2.54, 3.53, and 4.50 Hz, respectively. The first three natural frequencies of the 10-story building structure alone are 1.00, 2.96, and 4.86 Hz. The damping ratio for all modes of the buildings is assumed to be 2%. In this study, the wind load was restricted to the along-wind direction. Also, the influence of the relative locations of adjacent buildings on the wind load and each building's response was not considered.

5.3. Alternative solutions for locating the dampers

Solutions for different numbers and voltages of dampers (types of dampers) are now evaluated with respect to performance requirements for both earthquake and wind loads. The intent is to illustrate that solutions obtained by considering only a single dominant hazard (whether earthquake or wind) are quite different from each other as well as from solutions obtained by considering both hazards in combination. Overall, the problem of arriving at the number of dampers, voltage requirements, and their floor locations is an optimization problem whose solutions would vary with the design constraints imposed by the designer. In this study we consider three different types of solutions by considering different constraints: (i) Case-1: dampers are located on all floors and their number does not change from floor to floor; (ii) Case-2: dampers are located on only a single floor; and (iii) Case-3: the most general case in which the number of dampers can vary from floor to floor. In all cases, the voltage requirements remain the same for all the dampers.

Case-1: In this scenario, a fixed number of MR dampers with the same input voltage are used to connect the buildings on all ten floors. The design variables are defined as the number of dampers on each floor and the specific value of the input voltage. It must be noted that these design variables decide the damper force characteristics and correspondingly the total cost of the dampers. As this problem is characterized by only two design variables, a graphical representation is simple and helps in understanding and assessing the possible alternatives. The responses for the coupled buildings with MR dampers as characterized by Eq. (17) are computed numerically for both the earthquake and the wind time history loadings. Fig. 14 shows the contours of maximum inter-story drift under earthquake loading (R_e) and those of the

maximum along-wind acceleration under wind loading (R_w) for the coupled building structures. The contours are plotted by varying the number of dampers at each floor as well as the input voltage for the dampers. We make three main observations from this figure: (1) The solution for "zero" dampers, the case in which the buildings are not connected by dampers (i.e., both buildings independently), does not satisfy the performance requirements, thereby making it essential that the buildings be connected through dampers in order to withstand both the hazards. (2) There exists an optimal value of design variables, the number of dampers at each floor and the input voltage, which minimizes both R_e and R_w. Yet, the optimal design values are different under earthquake loading when compared to the corresponding values for the wind loading. (3) It is possible to obtain the optimal values of design variables that meet performance requirements for both the earthquake and the wind hazards and, at the same time, minimize the cost of dampers. For example, if the input voltage is assumed to be fixed at 2 V, then an optimum can be obtained as "3" which means 3 dampers at each of the 10 floors leading to a total of 30 dampers. It is apparent from Fig. 14 that this damper design can fulfill both performance requirements (dashed lines) and minimize the total number of dampers. This optimal solution for the multi-hazard scenario is quite different from the optimal solutions obtained for the single individual hazards of the earthquake or the wind.

Case-2: Klein and Healy [51] conclude that buildings having different natural frequencies should be connected near the top to ensure appropriate utilization of control devices, since the vibratory modes will most likely have nonzero amplitudes at the top. In our study, MR dampers are assumed to be installed between the 10th floors of the two buildings, which is obviously the top floor of the 10-story building. The two design variables for this case are the number of dampers on the 10th floor and the input voltage. Fig. 15 illustrates the contours for the R_e and R_w values of the coupled building structures with respect to the number of dampers and the input voltage. This figure is quite similar to Fig. 14 for Case-1 and the three main observations made in Case-1 also carry over to Case-2. A comparison of Case-1 and Case-2 shows that if the input voltage is fixed at 2 V, then the optimal number of dampers is **"18"** for Case-2 which is about one-third less than the total of 30 dampers needed in Case-1.

Case-3: As mentioned earlier, this case corresponds to allowing different numbers of dampers to be placed at different floors. Unlike the previous two cases, this case has more than two design variables, i.e., the total number of design variables is equal to the number of connected floors (to determine different number dampers needed at each floor) plus one additional variable for the input voltage. Therefore, there exists a total of 11 design variables in this scenario, which makes a graphical representation and determination of the potential solution quite difficult. Therefore, the problem is formulated as follows for a fixed input voltage value:

$$\begin{aligned} &\underset{\mathbf{x}}{\text{Minimize}}\ f(\mathbf{x}) = \sum_{i=1}^{10} x_i \\ &\text{Subject to } R_e \leqslant L_e;\ R_w \leqslant L_w \end{aligned} \tag{26}$$

where $f(\mathbf{x})$ is a total number of dampers and x_i is the number of dampers installed at the i^{th} floor. This optimization problem is solved to determine the optimal distribution for the number of MR dampers that can satisfy performance requirements for both the earthquake and wind hazards as well as minimize the total number of the dampers, as shown in Fig. 16(c). For comparison purposes, Fig. 16 also gives the distributions of the number of MR dampers and corresponding maximum responses (R_e and R_w) obtained from the Case-1 and Case-2. As seen in this figure, the total numbers of MR dampers for the Case-2 and the Case-3 are not much different from each other. We attribute this to the fact that, for Case-3, most of the MR dampers are located on the two top floors of the 10-story building. These observations can be used to conclude that it is most desirable to locate the dampers as close to the top floors of a building as possible.

6. Summary and conclusions

A performance-based framework is presented that determines whether the design and retrofit of given building types are governed by a single dominant hazard or instead by multiple hazards. While the study focuses on earthquake and wind hazards, the proposed framework is quite general in nature and can be applied to other external hazards as well. The performance criteria for each hazard can be different and can cover the various requirements of strength and serviceability. Besides, a single hazard can have two or more different performance limits, and such a feature can also be included. The framework is well suited for integration into the actively growing research area of probabilistic risk assessment. At the same time, we demonstrate that it can easily be converted to deterministically characterized performance criteria in accordance with deterministic demand and capacity requirements as specified traditionally in the various building codes and standards. Application of the framework to three different geographic locations in the United States demonstrates the significance of location in multi-hazard risk assessment. In addition, the significance of multi-hazard design considerations is illustrated through explorations of alternative retrofit solutions in two adjacent buildings located in close proximity to each other, such as those encountered in a tight urban setting. The particular example considered for a retrofit solution has been studied by other researchers and involves connecting the buildings through supplemental damping devices. We observe that the number of dampers and their locations—as determined from multi-hazard design considerations—are very different from those determined for a single dominant hazard. A related observation is that a solution that might satisfy the performance requirements for an earthquake is not necessarily acceptable with respect to the performance requirements for wind and vice-versa. More generally, it is clear that the process of determining risk is highly dependent upon three primary concerns: performance criteria, building geometry, and geographic location.

Declaration of Competing Interest

The authors declare that they have no known competing financial interests or personal relationships that could have appeared to influence the work reported in this paper.

Acknowledgements

This research was partially supported by the Center for Nuclear Energy Facilities and Structures at North Carolina State University. Resources for the Center come from the dues paid by member organizations and from the Civil, Construction, and Environmental Engineering Department and College of Engineering in the University.

References

[1] Kappes MS, Keiler M, von Elverfeldt K, Glade T. Challenges of analyzing multi-hazard risk: a review. Nat Hazards 2012;64(2):1925–58.
[2] Barbato M, Li Y, Padgett J. Recent advances in assessment and mitigation of multiple hazards. ASCE J Struct Eng 2017;143(9):02017001.
[3] Choi E, Ha J, Hahm D, Kim M. A Review of Multihazard Risk Assessment: Progress, Potential, and Challenges in the Application to Nuclear Power Plants. Int J Disaster Risk Reduct 2020;53:101933.
[4] Rathje EM, Saygili G. Probabilistic assessment of earthquake-induced sliding displacements of natural slopes. Bull New Zealand Soc Earthquake Eng 2009;42(1):18.
[5] Asprone D, Jalayer F, Prota A, Manfredi G. Proposal of a probabilistic model for multi-hazard risk assessment of structures in seismic zones subjected to blast for the limit state of collapse. Struct Saf 2010;32(1):25–34.
[6] Wang J, Gu X, Huang T. Using Bayesian networks in analyzing powerful earthquake disaster chains. Nat Hazards 2013;68(2):509–27.
[7] Kwag S. Probabilistic Approaches for Multi-Hazard Risk Assessment of Structures and Systems. PhD dissertation. Raleigh, NC: North Carolina State University; 2016.

[8] Kwag S, Gupta A. Bayesian network technique in probabilistic risk assessment for multiple hazards. Proceedings of 24th International Conference on Nuclear Engineering (ICONE 24), Charlotte, NC, US; June 26-30, 2016.
[9] Rosowsky DV, Mudd L, Letchford C. Assessing climate change impact on the joint wind-rain hurricane hazard for the northeastern US coastline. *In Risk analysis of natural hazards*. Cham: Springer; 2016. p. 113–34.
[10] Nguyen Sinh H, Lombardo FT, Letchford CW, Rosowsky DV. Characterization of joint wind and ice hazard in Midwestern United States. Nat Hazard Rev 2016;17(3):04016004.
[11] Kwag S, Gupta A. Probabilistic risk assessment framework for structural systems under multiple hazards using Bayesian statistics. Nucl Eng Des 2017;315(4):20–34.
[12] Kwag S, Hahm D. Development of an earthquake-induced landslide risk assessment approach for nuclear power plants. Nucl Eng Technol 2018;50(8):1372–86.
[13] Ellingwood BR. Acceptable risk bases for design of structures. Prog Struct Mat Eng 2001;3(2):170–9.
[14] Li Y, Ellingwood B. Framework for Multihazard Risk Assessment and Mitigation for Wood-Frame Residential Construction. ASCE J Struct Eng 2009;135(2):159–68.
[15] Potra FA, Simiu E. Multihazard design: structural optimization approach. J Optim Theory Appl 2010;144(1):120–36.
[16] Beavers JE et al., Multihazard issues in the central united states: Understanding the hazards and reducing the losses. ASCE Council on Disaster Risk Management Monograph No. 3, Reston, VA; 2009.
[17] Kameshwar S, Padgett JE. Multi-hazard risk assessment of highway bridges subjected to earthquake and hurricane hazards. Eng Struct 2014;78(1):154–66.
[18] Salman AM, Li Y. Multihazard Risk Assessment of Electric Power Systems. ASCE J Struct Eng 2016 Oct;20:04016198.
[19] Kwag S, Ha JG, Kim MK, Kim JH. Development of Efficient External Multi-Hazard Risk Quantification Methodology for Nuclear Facilities. Energies 2019;12(20):3925.
[20] Ni YQ, Ko JM, Ying ZG. Random seismic response analysis of adjacent buildings coupled with non-linear hysteretic dampers. J Sound Vib 2001;246(3):403–17.
[21] Bhaskararao AV, Jangid RS. Seismic response of adjacent buildings connected with friction dampers. Bull Earthq Eng 2006;4(1):43–64.
[22] Ok SY, Song J, Park KS. Optimal design of hysteretic dampers connecting adjacent structures using multi-objective genetic algorithm and stochastic linearization method. Eng Struct 2008;30(5):1240–9.
[23] Lee DG, Kim HS, Ko H. Evaluation of coupling–control effect of a sky-bridge for adjacent tall buildings. Struct Des Tall Special Build 2012;21(5):311–28.
[24] Kim HS, Kang JW. Semi-active fuzzy control of a wind-excited tall building using multi-objective genetic algorithm. Eng Struct 2012;41:242–57.
[25] Hart GC, Jain A. Performance-based wind evaluation and strengthening of existing tall concrete buildings in the Los Angeles region: dampers, nonlinear time history analysis and structural reliability. Struct Des Tall Special Build 2014;23(16):1256–74.
[26] Zheng C, Xie Y, Khan M, Wu Y, Liu J. Wind-induced responses of tall buildings under combined aerodynamic control. Eng Struct 2018;175:86–100.
[27] Raheem SEA, Fooly MY, Shafy AGA, Taha AM, Abbas YA, Latif MMA. Numerical simulation of potential seismic pounding among adjacent buildings in series. Bull Earthq Eng 2019;17(1):439–71.
[28] Zhu Z, Lei W, Wang Q, Tiwari N, Hazra B. Study on wind-induced vibration control of linked high-rise buildings by using TMDI. J Wind Eng Ind Aerodyn 2020;205:104306.
[29] ASCE. Minimum design loads for buildings and other structures, ASCE/SEI 7-05/-10, Reston, VA, US.
[30] Wen YK, Kang YJ. Minimum building life-cycle cost design criteria. I: Methodology. ASCE J Struct Eng 2001;127(3):330–7.
[31] Duthinh D, Simiu E. Safety of structures in strong winds and earthquakes: multihazard considerations. ASCE J Struct Eng 2009;136(3):330–3.
[32] Crosti C, Duthinh D, Simiu E. Risk consistency and synergy in multihazard design. ASCE J Struct Eng 2010;137(8):844–9.
[33] Chen EY. Multi-hazard design of mid- to high-rise structures. M.S. thesis. Urbana-champaign, IL: Univ. of Illinois; 2012.
[34] Li Y, Ahuja A, Padgett J. Review of methods to assess, design for, and mitigate multiple hazards. ASCE J Perform Constructed Facilities 2012;26(1):104–17.
[35] AIA, Buildings at Risk: Multihazard Design for Earthquakes, Winds and Floods, The American Institute of Architects, NW Washington, DC, US; 1997.
[36] Unobe ID, Sorensen AD. Multi-hazard analysis of a wind turbine concrete foundation under wind fatigue and seismic loadings. Struct Saf 2015;57:26–34.
[37] IBC 2012, International Building Code, International Code Consortium.
[38] Tallin A, Ellingwood B. Wind induced lateral-torsional motion of buildings. ASCE J Struct Eng 1985;111(10):2197–213.
[39] Kwok KC, Burton MD, Abdelrazaq AK. *Wind-induced motion of tall buildings: designing for habitability*. American Society of Civil Engineers; 2015.
[40] Burton MD, Kwok KC, Abdelrazaq A. Wind-induced motion of tall buildings: designing for occupant comfort. Int J High-Rise Build 2015;4(1):1–8.
[41] Mohsenian V, Gharaei-Moghaddam N, Hajirasouliha I. Multilevel seismic demand prediction for acceleration-sensitive non-structural components. Eng Struct 2019;200:109713.
[42] Gandelli E, Taras A, Distl J, Quaglini V. Seismic retrofit of hospitals by means of hysteretic braces: influence on acceleration-sensitive non-structural components. Front Built Environ 2019;5:100.
[43] Gasparini DA, Vanmarcke EH. Simulated earthquake motions compatible with prescribed response spectra. *Civil Engineering Research Report R76–4*. Cambridge, USA: Massachusetts Institute of Technology; 1976.
[44] Wittig LE, Sinha AK. Simulation of Multicorrelated Random Processes using the FFT Algorithm. J Acoust Soc Am 1975;58(3):630–3.
[45] Dyrbye C, Hansen SO. Wind Loads on Structures. New York: John Wiley & Sons Ltd; 1997.
[46] Zhou Y, Kijewski T, Kareem A. Aerodynamic Loads on Tall Buildings: An Interactive Database. ASCE J Struct Eng 2003;129(3):394–404.
[47] Spencer Jr BF, Dyke SJ, Sain MK, Carlson JD. Phenomenological model of magnetorheological damper. ASCE J Eng Mech 1997;123(3):230–8.
[48] Dyke SJ, Spencer Jr BF, Sain MK, Carlson JD. An experimental study of MR dampers for seismic protection. Smart Mater Struct 1998;7(5):693–703.
[49] Barber TT, Wen YK. Random vibration of hysteretic, degrading systems. ASCE J Eng Mech Division 1981;107(6):1069–87.
[50] Yi F, Dyke SJ, Caicedo JM, Carlson JD. Experimental verification of multi-input seismic control strategies for smart dampers. ASCE J Eng Mech 2001;127(11):1152–64.
[51] Klein RE, Healey MD. Semi-active control of wind induced oscillations in structures. Proceeding for 2nd International Conference on Structural Control, Univ. of Waterloo, Ontario, Canada, Martinus Nijhoff Publishers, Dordrecht, Netherlands; 1987. p. 354-369.